

Design and experiment of a large-scale space micro-vibration simulator

He Zhu^{1,2}, Shuai He¹, Junli Shen¹, Mingyi Xia¹, Chao Qin¹, Xiaoming Wang¹, Xiangyang Sun^{1,2} and Zhenbang Xu¹

Journal of Vibration and Control
2024, Vol. 30(3-4) 740–752
© The Author(s) 2023
Article reuse guidelines:
sagepub.com/journals-permissions
DOI: 10.1177/10775463221150825
journals.sagepub.com/home/jvc



Abstract

To solve the problems of difficult vibration sources simulation in the ground test of the on-orbit optical load, a multi-dimensional micro-vibration simulator based on the improved Gough–Stewart platform was designed, which can effectively reproduce the characteristics of wide frequency distribution and small vibration magnitude of space micro-vibration. The analytical formula was derived by using the virtual frequent principle and the Newton–Euler equation for the natural frequency of the system, and the simulator’s configuration was optimized. The structure of legs was designed and optimized according to the optimal configuration parameters. Finally, the micro-vibration simulator was tested, and the test results showed that the output bandwidth of the simulator was 5–300 Hz and the maximum magnitude error was 8%, thus demonstrating the multi-dimensional micro-vibration simulation platform has the characteristics of large frequent bandwidth, high load carrying capacity, and small vibration magnitude.

Keywords

space micro-vibration, simulator, transfer function

1. Introduction

During the on-orbit operation of spacecraft, the space micro-vibrations will be generated by on-board motion equipment and devices in spacecraft. With the improvement of the observation resolution of the space optical remote sensors, the micro-vibration of satellite platform gives increasingly prominence to the restrictive effects of remote sensor imaging performance index (Hadar et al., 1992; Le et al., 2013; Liu et al., 2015; Serief et al., 2017). Therefore, in order to further improve the observation performance of space remote sensors, it is necessary to carry out research on the adaptability of space remote sensors to the micro-vibration environment of the satellite platform, fully grasp the characteristics of the satellite platform micro-vibration and the mechanism of the platform micro-vibration influence on the image quality of the space remote sensors, and then study the corresponding strategies to overcome or weaken the adverse effects of the satellite platform micro-vibration on the image quality of the space remote sensors and improve the observation accuracy.

At present, researchers have carried out a lot of researches on micro-vibration. Laskin and Martin (1989) concluded that the Reaction Wheel Assembly (RWA) and Control Momentum Gyros (CMG) are the largest micro-vibration disturbance sources. Cui et al. (2019) analyzed the influencing characteristic of micro-vibration on imaging

quality from the aspects of micro-vibration’s direction, amplitude, frequency, and phase. Lin et al. (2018) studied the impact of flywheel micro-vibration on a high resolution optical satellite that space-borne integrated. To deeply study the working state of payload in the space micro-vibration environment, it is necessary to carry out a ground micro-vibration test to simulate the space micro-vibration environment. Two methods can be adopted to simulate the micro-vibration environment: one is to use real disturbance equipment (Zhou et al., 2011; Wu et al., 2019), in which the simulated disturbance source is relatively single and it will

¹Innovation Lab of Space Robot System, Space Robotics Engineering Center, Changchun Institute of Optics, Fine Mechanics and Physics, Chinese Academy of Sciences, Changchun, China

²University of Chinese Academy of Sciences, Beijing, China

Received: 1 September 2022; accepted: 19 December 2022

Corresponding authors:

Shuai He, Changchun Institute of Optics Fine Mechanics and Physics Chinese Academy of Sciences, No. 3888 Dong Nanhu Road, Changchun, Jilin 130033, China.
Email: 652740868@qq.com

Zhenbang Xu, Changchun Institute of Optics Fine Mechanics and Physics Chinese Academy of Sciences, No. 3888, Southeast Lake Road, Erdao District, Changchun City, Jilin 130033, China.
Email: xuzhenbang@ciomp.ac.cn

also be affected by production scheduling; the other is to design the micro-vibration simulator which can simulate the various disturbance sources. Since spacecraft and its payload are usually in a multi-DOF space micro-vibration environment (Lee-Glauser et al., 1994; Whiteman et al., 2014), it is particularly important to design a multi-DOF micro-vibration simulator.

There are also many achievements in micro-vibration simulation platform. Park et al. (2012, 2014) proposed the disturbance force simulator which only stayed in the theoretical stage. The University of Pennsylvania designed the novel micro-vibration simulators based on the Gough–Stewart configuration (Vose et al., 2009, 2013). The Gough–Stewart platform (GSP) has characteristics including high rigidity, a stable structure, and good dynamic performance, so it often used as the space micro-vibration simulator (Shao et al., 2012; Joshi et al., 2004; Tang et al., 2013). Wang et al. (2017) proposed a multi-degree-of-freedom simulator based on the GSP that can exactly produce the required micro-vibration spectrum. Yang et al. (2016) proposed a novel acceleration simulator which can reproduce 6-DOF micro-vibrations with different amplitudes and frequencies. However, they only stayed in the simulation stage and did not show the real object of the simulator.

Though the GSP is widely used in the micro-vibration field, the conventional Gough–Stewart configuration platforms suffer from two major drawbacks: the first is the mass and stiffness of the legs can result in spurious resonances, and the second is the conventional rotational joints suffer from the problem of friction and backlash (Verma et al., 2020) which degrades the performance. In order to derive good performance of the 6-DOF micro-vibration simulator, the structural parameters need to be optimized. Wang et al. (2018) designed and tested leaf springs of the driving leg and gimbals to improve performance of simulator's legs. He et al. (2017) improved the micro-vibration simulator's performance by designing and optimizing driving legs, hinges, upper platform and lower platform. However, their simulator's bandwidth was not high enough. In order to increase the simulation bandwidth and inherence the performance, it is necessary to design and optimize the simulator.

In this study, a multi-degree-of-freedom micro-vibration simulator based on the GSP, which can exactly reproduce the six-dimensional acceleration, is presented. The dynamic model is established to calculate the natural frequency of the system; then the optimal configuration parameter is obtained by configuration optimizing and used for the structure design to increase the bandwidth of the simulator; finally, the iterative feedback control strategy is used to control the simulator to provide the 6-DOF micro-vibration test. Compared with the previous simulator (Zhu et al., 2022), it can be seen that simulator proposed in this paper has the characteristics of larger frequent bandwidth, higher

load carrying capacity and can simulate smaller vibration magnitude.

The paper is organized as follows. Section 2 of the paper introduces the configuration optimization of the improved Gough–Stewart platform. Section 3 designs and optimizes the structure of the platform. Section 4 presents experimental measurements of the six-dimensional acceleration that are produced by the simulator. Section 5 draws conclusions about the performance of the 6-DOF micro-vibration simulator.

2. Configuration optimization

In this section, a six-dimensional parallel platform based on an improved Stewart–Gough configuration is proposed. For such mechanism, the configuration parameters determine the first six natural frequency of the simulator and the lowest frequency of the analog bandwidth. Therefore, the natural frequency analytical formula of the system will be obtained by theoretical modeling, and subsequently the optimal configuration parameters are obtained by traversing optimization, which provides a basis for the structure design of the simulator.

2.1. Theoretical modeling

The diagram of the parallel platform and the single leg is shown in Figure 1. The geometric parameters for determining the platform configuration are: the upper platform radius R_P , the base platform radius R_B , the upper and base platform central angles at hinge point α and β , and the height of the origin of the body frame in the base frame H . The entire platform consists of upper platform, base platform, and six identical legs which is composed of an actuator (indicated by a sliding pair) and a connecting rod. Each actuator is fixed to the lower platform, and the connecting points are represented by B_i ($i = 1-6$). The upper joint points on the upper platform represent that connecting rods are connected to the upper platform by hinges and are given by p_i ($i = 1-6$), and the lower joint points on the actuators represent that connecting rods are connected to the actuators by hinges and are given by U_i ($i = 1-6$). The $\{P\}$ coordinate system is used to represent the body frame, while the $\{B\}$ coordinate system represents the base frame. $q = [x \ y \ z \ \phi \ \varphi \ \eta]^T$ is the position matrix of the body frame $\{P\}$, and the rotation matrix of the transformation from the body frame $\{P\}$ to base frame $\{B\}$ is given by

$${}^B_P R = \begin{bmatrix} c\varphi c\eta & c\eta s\varphi s\phi - s\eta c\phi & c\eta s\varphi c\phi + s\eta s\phi \\ s\eta c\varphi & s\eta s\varphi s\phi + c\eta c\phi & s\eta s\varphi c\phi - c\eta s\phi \\ -s\varphi & c\varphi s\phi & c\varphi c\phi \end{bmatrix} \quad (1)$$

where $s(\cdot) = \sin(\cdot)$, $c(\cdot) = \cos(\cdot)$.

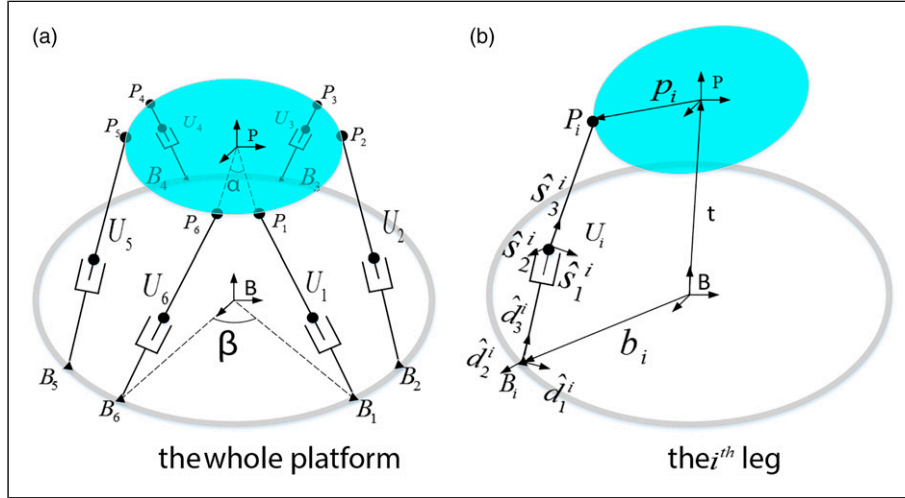


Figure 1. Diagram of the 6-DOF micro-vibration platform: (a) the whole platform and (b) the i^{th} leg.

Frame \hat{d}^i is the reference frame which is attached to the base platform at B_i with \hat{d}_3^i along the i^{th} actuator. The hat ($\hat{\cdot}$) above the variables indicates that it is a unit of length. The \hat{s}^i coordinate system is located on the i^{th} rod at the center of mass of the lower joint with \hat{s}_3^i along the i^{th} rod, and the length vector l_{BP}^i of the leg can be expressed as follows

$$l_{BP}^i = {}^B t + {}^B p_i - {}^B b_i = {}^B t + {}^B_p R \cdot {}^P p_i - {}^B b_i \quad (2)$$

Taking the derivative of equation (2) with respect to time, the velocity mapping function v_{pi} can be obtained as

$$v_{pi} = \dot{l}_{BP}^i = \dot{{}^B t} + \omega \times {}^B_p R {}^P p_i = \left[I_3, {}^B_p R \left({}^P \tilde{p}_i \right)^T {}^P p_i^T \right] \dot{q} = J_{pi,q} \cdot \dot{q} \quad (3)$$

where $J_{pi,q}$ denotes a Jacobian matrix relating the general velocity to the velocity of the upper joint, $J_{pi,q} = [E_3, {}^B_p R \left({}^P \tilde{p}_i \right)^T {}^P p_i^T]$, and \dot{q} is the general velocity of the upper platform.

The length of the i^{th} rods and actuator are given by s_i and d_i , respectively. Equation (2) can be expressed as

$$l_{BP}^i = s_i \hat{s}_3^i + d_i \hat{d}_3^i \quad (4)$$

Dot-multiplying both sides of equation (4) by $s_i \hat{s}_3^i$ gives

$$s_i^2 = (l_{BP}^i - d_i \hat{d}_3^i)^T (l_{BP}^i - d_i \hat{d}_3^i) = l_{BP}^{i2} - 2d_i \hat{d}_3^{iT} l_{BP}^i + d_i^2 \quad (5)$$

Solving equation (5), the length d_i of the rod can be obtained as

$$d_i = \hat{d}_3^{iT} l_{BP}^i - \sqrt{(\hat{d}_3^{iT} l_{BP}^i)^2 - l_{BP}^{i2} + s_i^2} \quad (6)$$

Taking the derivative of both sides of equation (6) with respect to time, and simplifying, the sliding velocity of the actuator can be described by

$$\dot{d}_i = (l_{BP}^i - d_i \hat{d}_3^i)^T (J_{pi,q} \dot{q}) / [(l_{BP}^i - d_i \hat{d}_3^i)^T \hat{d}_3^i] \quad (7)$$

Based on their physical meaning, the velocities of the upper joint p_i can also be described in terms of the velocity of the centroid of the actuator and the angular velocity of the rod ω_{si} under frame $\{B\}$ as

$$v_{pi} = \dot{d}_i \hat{d}_3^i + \omega_{si} \times (s_i \hat{s}_3^i) \quad (8)$$

According to equations (3) and (8), the following expression can be obtained

$$s_i \omega_{si} \times \hat{s}_3^i = \dot{l}_{BP}^i - \dot{d}_i \hat{d}_3^i \quad (9)$$

Pre-multiplying both sides of equation (22) with \hat{s}_3^i yields

$$\dot{d}_i = \hat{s}_3^{iT} \cdot \dot{l}_{BP}^i + \left[({}^B_p R \cdot {}^P p_i) \times \hat{s}_3^i \right]^T \omega \quad (10)$$

The six legs are considered simultaneously, and equation (10) can be expressed

$$\dot{D} = J_{d,q} \cdot \dot{q} \quad (11)$$

where $\dot{D} = [\dot{d}_1 \ \dot{d}_2 \ \dot{d}_3 \ \dot{d}_4 \ \dot{d}_5 \ \dot{d}_6]$ and $J_{d,q} = [\hat{s}_3^{iT}, [({}^B_p R \cdot {}^P p_i) \times \hat{s}_3^i]^T] / (\hat{s}_3^{iT} \hat{d}_3^i)$ denote the Jacobian matrix relating the general velocity to the sliding velocity of the actuator.

Combined with Virtual Work Principle, the upper platform is pressed with an external force F

$$F^T \cdot \Delta q = f^T \cdot \Delta D \tag{12}$$

where f is the output force matrix of six actuators, and when the axial stiffness is k

$$f = k \cdot \Delta D \tag{13}$$

According to equations (11) ~ (13), F can be obtained

$$F = k \cdot J_{d,q}^T \cdot J_{d,q} \cdot \Delta q \tag{14}$$

The generalized stiffness matrix of the platform can be expressed as

$$K = k \cdot J_{d,q}^T \cdot J_{d,q} \tag{15}$$

According to the Newton–Euler equation, the natural frequency of the platform can be obtained by solving the following equation (16)

$$\|K - \omega^2 M\| = 0 \tag{16}$$

where $M = \begin{bmatrix} mI_3 & m \cdot {}^B_p R \cdot {}^P \tilde{P}_C^T \cdot {}^B_p R^T \\ m \cdot {}^B_p R \cdot {}^P \tilde{P}_C^T \cdot {}^B_p R^T & {}^B_p R \cdot {}^P I \cdot {}^B_p R^T \end{bmatrix}$ denotes

the generalized mass of platform, ${}^P I$ is the inertia tensor of the upper platform under frame $\{P\}$, and ${}^P \tilde{P}_C$ is the skew symmetric matrix of the comprehensive centroid of the upper platform and the load in the body frame.

2.2. Parameter optimization

It is supposed that the bandwidth of the simulator can reach 5–300 Hz and avoid resonance, the first 6-order natural frequencies of the system is required to be as low as possible, and the 7th-order natural frequency is supposed to be as high as possible. The paper (Xin et al., 2015) shows that the 7th mode is a local lateral swing caused by the spring leaf’s bending stiffness. The larger the bending stiffness, the larger the 7th natural frequency. For the spring leaf with a certain section shape, the bending stiffness increases as the axial stiffness increases. Therefore, the aim of configuration optimization is to make the spring leaf’s axial stiffness as large as possible within limits, and the constraint condition is that the sixth natural frequency is 3.5 Hz. The configuration optimization process is shown in Figure 2, the parameters optimization ranges and the optimal parameters are shown in Table 1, and the maximum axial stiffness $k_{max} = 55$ N/mm.

3. Design and optimization of structure

The structure is designed and optimized according to the optimal configuration parameters obtained in Section 2, and the 3-D model is shown in Figure 3. A parallel platform based on an improved Stewart–Gough configuration is used as the micro-vibration generator in this section. The connecting legs of the traditional Stewart–Gough platform is connected with the upper and lower platforms by hinges and the motor is installed on the each connecting legs. Relatively, the legs of improved Stewart–Gough configuration are connected to the upper platform by connecting rods and hinges, and the motor is fixed to a fixed mount, which can reduce the suspended mass attached to the legs and increase the bending frequency of the whole platform.

3.1. Design of spring leaf

A linear system is needed in the driving leg to ensure that the coil of the voice coil motor can move axially, which can be met by coaxially installing the three spring leaves in the driving leg. For the design of the spring leaf, it not only needs to ensure that the first 6 radical frequencies of the system are as small as possible but also needs to ensure that the 7th radical frequency as large as possible. Here, a design method based on the stiffness ratio Q (i.e., the ratio of bending stiffness to axial stiffness) is proposed. The Q value is only related to the spring leaf’s geometric shapes, and the larger the Q , the larger the 7th radical frequency of the legs when the first 6 radical frequencies are the same.

The spring leaf’s (circular) design parameters mainly include the inner radius $R1$, the outer radius $R2$, and the thickness t . When optimizing parameters, the influence of each parameter on the Q is shown in Figure 4. The Q value increases with the increase of $R1$ and $R2$, but the t has little effect on the Q .

According to the above relationship, $R2$ is defined as the dimensional constraint and the value of $R2-R1$ cannot be too small, otherwise local deformation of the spring leaf will occur; the spring leaf will have the lower local mode when the thickness t is too small, which will also affect the control bandwidth of the system. After optimization, the finally selected spring leaf’s parameters are $R1 = 37$ mm, $R2 = 79$ mm, $t = 0.22$ mm, and $Q = 1235$ mm²/rad. When the spring leaf moves axially by 2 mm, the maximum stress of the spring leaf is 213 MPa; therefore, the leaf spring will not be damaged during normal working.

3.2. Design of upper platform assembly

The upper platform assembly is composed of the payload platform, the upper spherical hinges, the upper mounting base, and the reinforcing plate, as shown in Figure 5(a). The payload platform is used as the space load test platform, the reinforcing plate is used to increase the natural frequency of

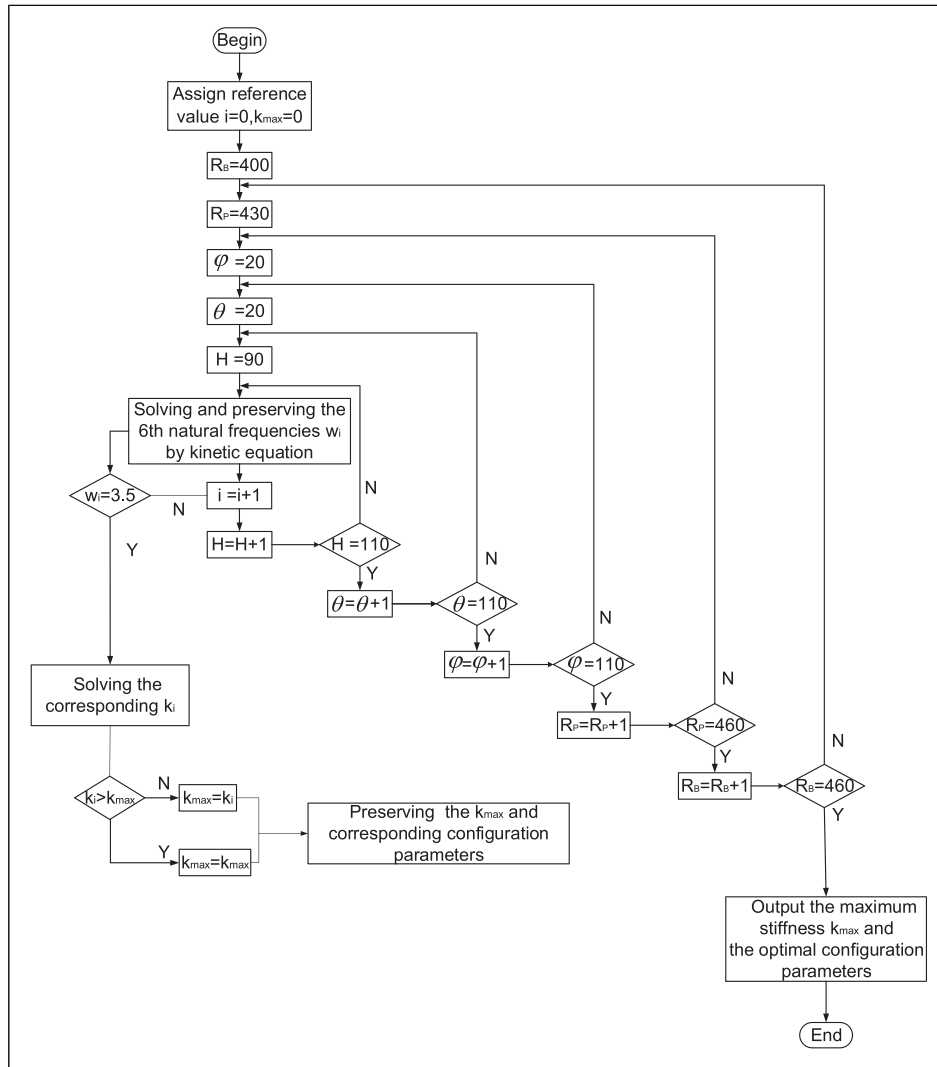


Figure 2. Configuration optimization process.

Table 1. Configuration parameters optimization.

	The base platform radius R_B (mm)	The upper platform radius R_p (mm)	The upper platform central angle at hinge point α ($^\circ$)	The base platform central angle at hinge point β ($^\circ$)	The height of the origin of the body frame in the base frame H (mm)
Optimization range	[400, 460]	[430, 460]	[20, 110]	[20, 110]	[90, 110]
Optimal parameters	460 mm	430 mm	102 $^\circ$	25 $^\circ$	102 mm

the upper platform, and the mounting base is used to connect the upper platform and the connecting rods.

To make the payload platform's natural frequency as high as possible, the height and thickness of the stiffener, the reinforcing plate and the upper platform plate thickness

(divided into three parts), etc., are optimized, as shown in Figure 5(b). The analysis results are shown in Figure 6:

- (a) The radical frequency of the payload platform decreases with the increase of plate 1 thickness and is less

affected by the thickness of plate 3; when the thickness of the mounting plate (i.e., plate 2) is small, the radical frequency of the payload platform increases obviously with the thickness of the mounting plate, and the latter will be close to convergence.

- (b) When the thickness of the stiffener is small, the radical frequency of the payload platform increases with the increase of the stiffener thickness, but the increase will get smaller and smaller and even be reduced.
- (c) On the studied interval, the radical frequency of the upper platform and the height of the stiffener are approximately linear.

The radical frequency of the upper platform is 466 Hz after optimization, and if the reinforcing plate is taken into consideration, the radical frequency will reach to 500 Hz. The optimized parameters are shown in Table 2.

3.3. Design of single-axis actuator

Figure 7 shows a 3-D structure view and cutaway view of a single-axis actuator. The single-axis actuator is divided into actuator part and fixed part. The actuator part includes the voice coil motor mover (coil), the excitation shaft, the spring leaf, the spherical hinge, and shims 1 and 3–5, and the fixed part includes the voice coil motor stator (permanent magnet), the motor base, insulating pad 2, and shim 2. The whole motor is connected with the motor base through the upper and lower spring leaves which are fixed by the shim on the excitation shaft. The three spring leaves in Section 3.1 are selected as the linear system in parallel, and it can improve the bending stiffness of the single-axis actuator by increasing the distance between the two spring leaves without changing the configuration parameters of the platform.

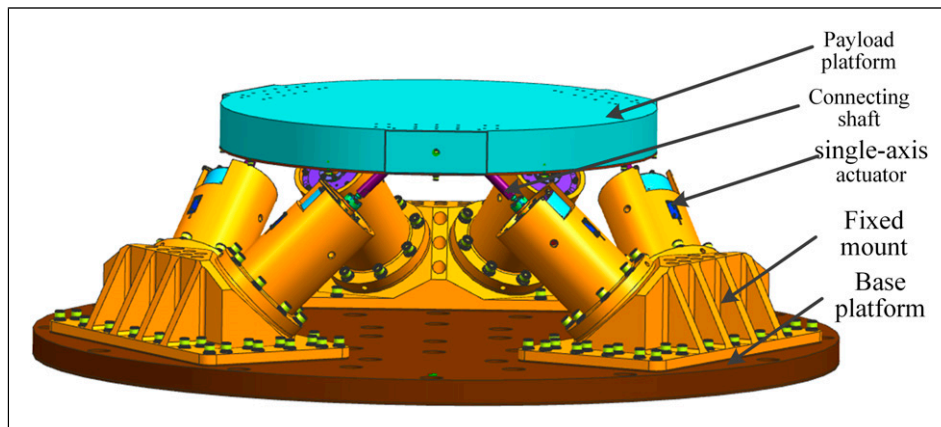


Figure 3. Space micro-vibration simulation platform.

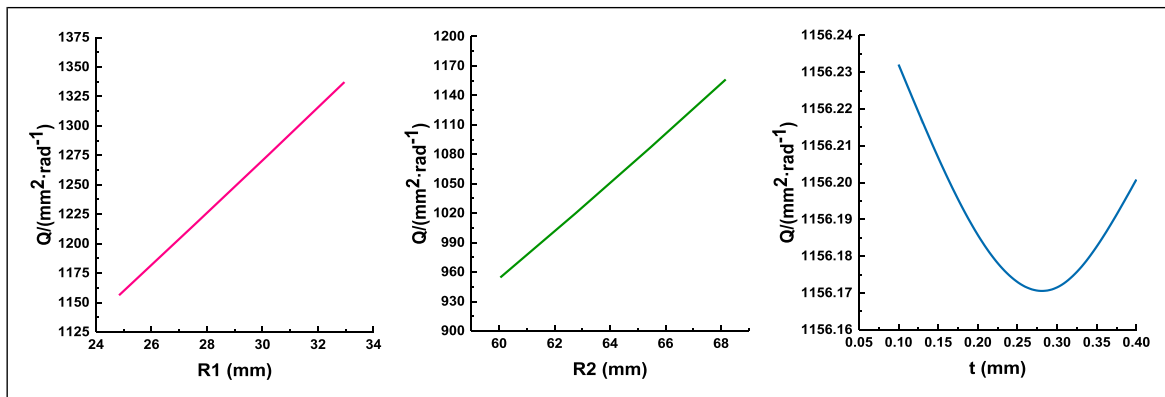


Figure 4. The influence of each parameter on the Q.

3.4. Optimization results

After completing the optimization of the simulator, the modal analysis of the whole platform is carried out by using the MSC/Nastran. The first 7 modes of the whole model with 300 kg load are shown in Figure 8. The first 3th and the 4th–6th natural frequency represents the translational and rotational motion of upper platform, respectively. The 7th natural frequency represents the local mode of 6 legs. As a result, the great difference between the 6th order (3.4 Hz) and the 7th order (356 Hz) natural frequencies can ensure that the

simulator can simulate the micro-vibration with large bandwidth without resonance.

4. Experiment

In this paper, an iterative control strategy based on transfer function is used to control the simulator, and the specific control methods can be found in literature (He et al., 2017). The complete machine test system is shown in Figure 9, and it includes the micro-vibration simulator, the gravity unloading system, the Beckhoff system,

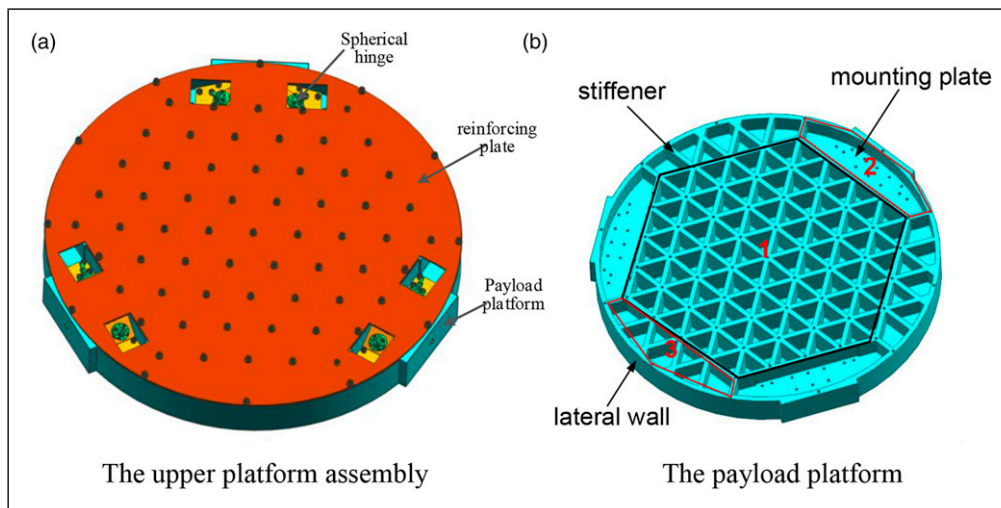


Figure 5. The structure of upper platform: (a) the upper platform assembly and (b) the payload platform.

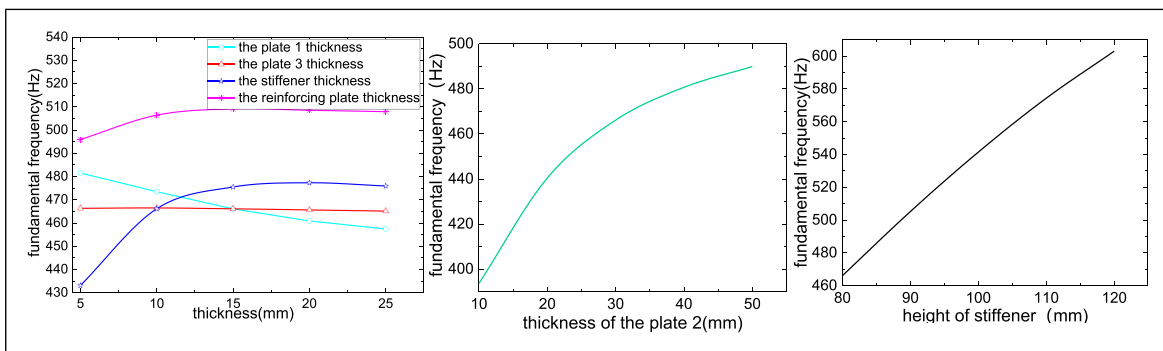


Figure 6. Effect of various parameters of the upper platform on the radical frequency.

Table 2. Optimized parameters.

The thickness of plate 1 (mm)	The thickness of plate 2 (mm)	The thickness of plate 3 (mm)	The height of stiffener (mm)	The thickness of stiffener (mm)	The thickness of reinforcing plate (mm)
20	40	40	80	15	5

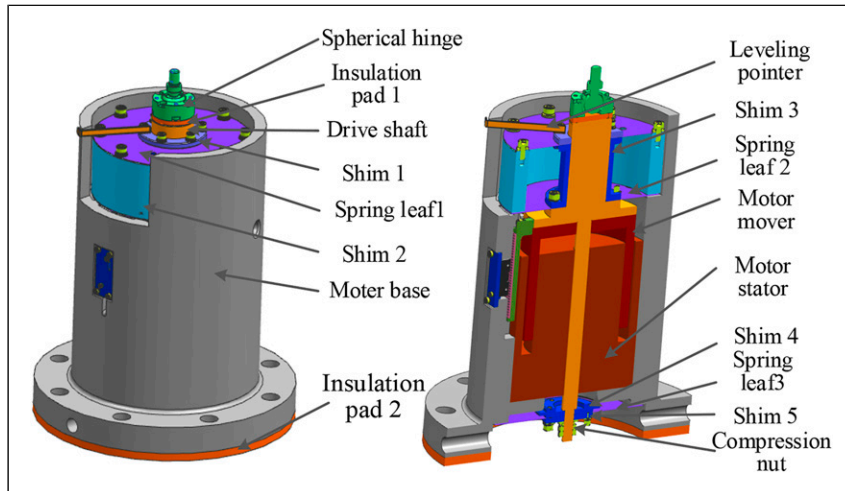


Figure 7. The single-axis actuator structure.

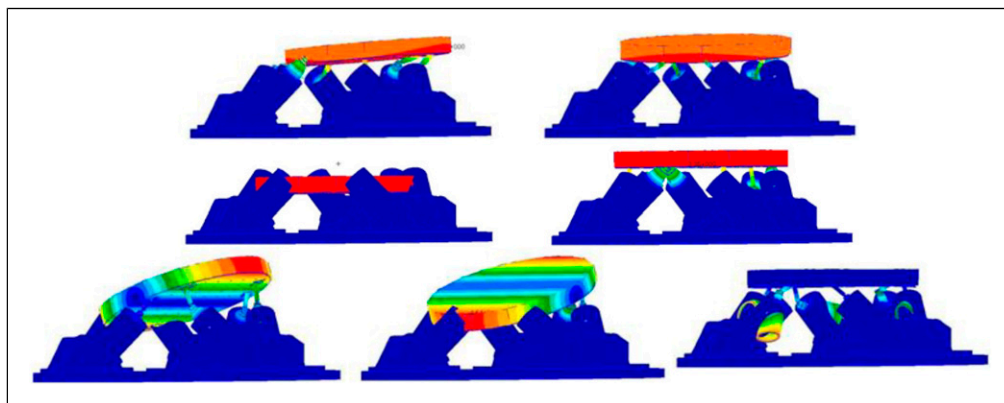


Figure 8. The first 7 mode figures of the whole platform model.

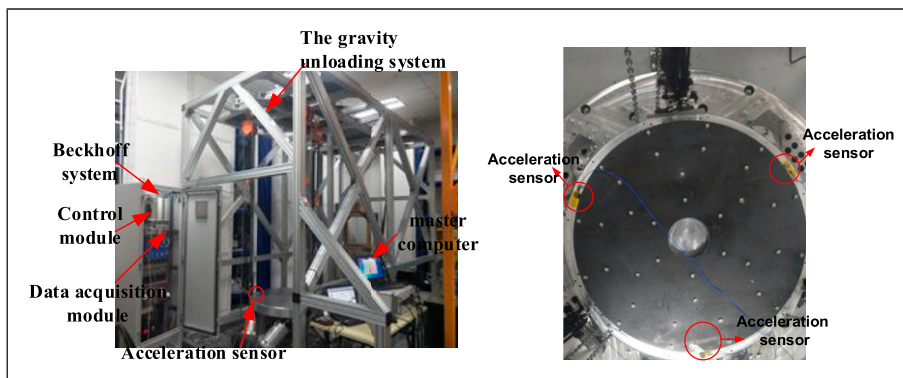


Figure 9. The complete machine test system.

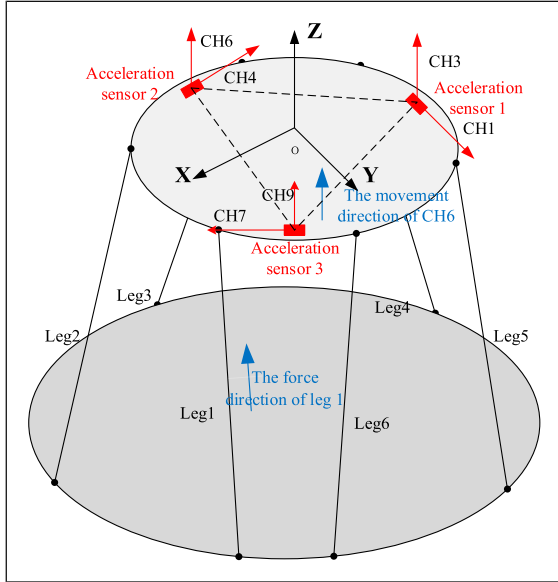


Figure 10. Position of legs and sensors in the test.

acceleration sensors, and the master computer, etc. The experimental procedure of system is as follows: the target accelerations are input at the master computer and then are converted by the control module of Beckhoff system into the corresponding force to drive the legs of simulator. Data acquisition module of the Beckhoff system collects the values of three acceleration sensors and feeds them back to the master computer.

4.1. Transfer function test

The sinusoidal excitation force with a fixed amplitude is applied to the six legs, and the transfer function of the upper platform's acceleration relative to the excitation force of each leg can be obtained by using the signal acquisition system to collect the input signal and the output signal of each acceleration sensors. At low frequencies, the structural damping coefficient of the system is small and the phase difference between the output signal and the input signal is near 0° or 180° ; therefore, the transfer function can be simplified from a complex matrix to a real matrix. The negative number in the real matrix represents a phase difference of 180° , and a positive number represents a phase difference of 0° .

The calibration matrix is represented by SIGN, and the number of each leg and the channel number of the sensor are shown in Figure 10. First, the single leg is driven to do sinusoidal motion, the time domain signal of each sensor is measured, and the calibration matrix is obtained according to the relative phase relationship of the curve. It can be seen from the statics that when a constant force is applied upward axially along leg 1, sensor 9 will move upward and the corresponding direction is

the positive direction of sensor 9. In the low-frequency non-damping sinusoidal motion, the excitation direction of leg 1 is consistent with the movement direction of sensor 9, so the relationship between the response and excitation force of sensor 9 is determined to be positive, corresponding to the sixth element of the first column in the calibration matrix. Figure 11 shows that the phase of sensor 1 and sensor 9 are opposite in the time domain response, so the relationship between sensor 1 response and excitation force is negative. Similarly, the calibration matrix of the response of all sensors relative to excitation forces can be obtained, which can be expressed as

$$\text{SIGN} = \begin{bmatrix} -1 & 1 & -1 & 1 & -1 & 1 \\ -1 & -1 & 1 & 1 & 1 & 1 \\ -1 & 1 & -1 & 1 & -1 & 1 \\ 1 & 1 & 1 & 1 & -1 & -1 \\ 1 & -1 & 1 & -1 & 1 & -1 \\ 1 & 1 & -1 & -1 & 1 & 1 \end{bmatrix} \quad (17)$$

The upper platform's transfer function is expressed as

$$H(\omega) = \text{SIGN} \times \begin{bmatrix} H_{11} & H_{12} & H_{13} & H_{14} & H_{15} & H_{16} \\ H_{21} & H_{22} & H_{23} & H_{24} & H_{25} & H_{26} \\ H_{31} & H_{32} & H_{33} & H_{34} & H_{35} & H_{36} \\ H_{41} & H_{42} & H_{43} & H_{44} & H_{45} & H_{46} \\ H_{51} & H_{52} & H_{53} & H_{54} & H_{55} & H_{56} \\ H_{61} & H_{62} & H_{63} & H_{64} & H_{65} & H_{66} \end{bmatrix} \quad (18)$$

The transfer function cannot be simplified when the frequency of excitation force is close to the higher order radical frequency of the system, and it is necessary to obtain the complete transfer function.

4.2. 6-DOF micro-vibration test

In fact, the space micro-vibration mainly exists in the form of line spectrum (Zhou, et al., 2012; Zhou, et al., 2013) and has the characteristics of large-magnitude at low-frequency and small-magnitude at high-frequency. Based on the above principles, the test conditions and test results are determined as shown in Table 3, where A_{Tx} , A_{Ty} , and A_{Tz} are the three translational acceleration trajectories at upper platform center point in units of mg and A_{Rx} , A_{Ry} , and A_{Rz} are the three angular acceleration trajectories at upper platform center point in units of μrad . In Table 3, the simplified transfer function is used and it does not need iterative processing in the frequency range prior to 100 Hz, and the iterative control method is adopted while using the simplified transfer functions in the frequency range between 100 Hz and 250 Hz. In the frequency range above 250 Hz, the result deviates significantly from the target value, and the complete transfer function is required.

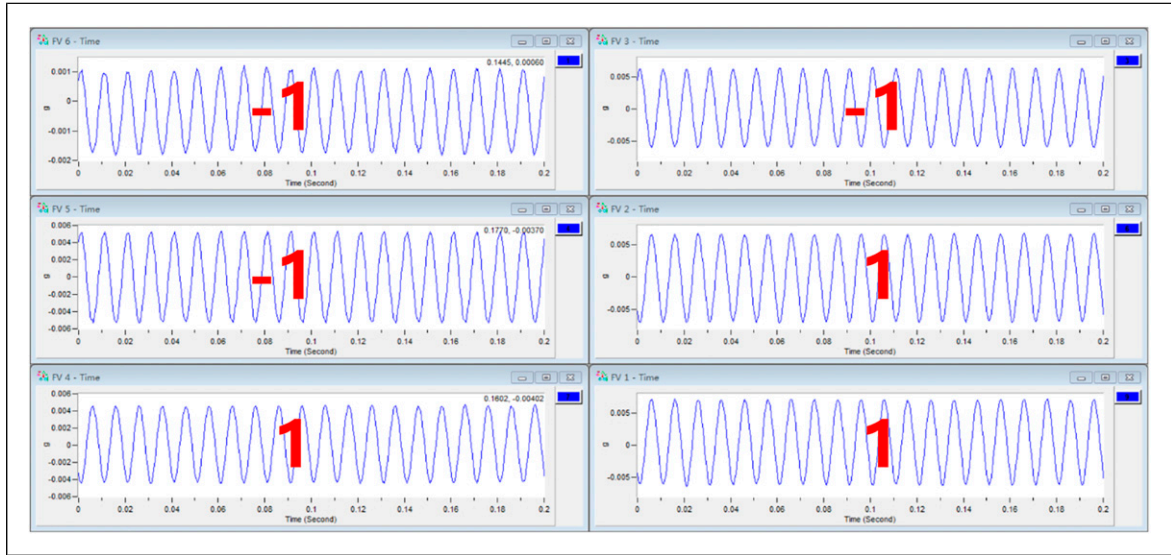


Figure 11. Time domain response curve of each acceleration channel when leg I is driven.

Table 3. The single-frequent and multi-frequent micro-vibration test results.

		Acceleration						
Frequency			A_{TX} (mg)	A_{TY} (mg)	A_{TZ} (mg)	A_{RX} (μ rad)	A_{RY} (μ rad)	A_{RZ} (μ rad)
Single-frequent test	5.0 (Hz)	Target acceleration	80	100	120	120	150	180
		Actual acceleration	80.83	101.64	119.36	120.24	151.08	179.62
		Magnitude error (%)	1.03	1.64	0.37	0.20	0.72	0.21
	63.8 (Hz)	Target acceleration	12	15	-16	8	3	-6
		Actual acceleration	12.51	15.33	-16.25	7.93	3.01	-6.11
		Magnitude error (%)	4.25	2.20	1.56	0.88	0.33	1.83
	100.0 (Hz)	Target acceleration	2	-2	-1	-1	1	1
		Actual acceleration	2.01	-1.98	-0.95	-1.06	1.02	0.99
		Magnitude error (%)	0.50	1.00	5.00	6.00	2.00	1.00
	160.0 (Hz)	Target acceleration	0.5	-0.5	0.5	0.05	-0.05	-0.05
		Actual acceleration	0.509	-0.502	0.499	0.051	-0.048	-0.05
		Magnitude error (%)	1.80	0.40	0.20	2.00	4.00	0.00
	254.4 (Hz)	Target acceleration	0.2	0.5	-2	-2	3.5	-0.1
		Actual acceleration	0.2027	0.502	-2.0216	-2.002	3.4843	-0.101
		Magnitude error (%)	1.35	0.40	1.08	0.10	0.45	0.10
	320.0 (Hz)	Target acceleration	0.1	0.1	-0.1	0.01	0.02	-0.03
		Actual acceleration	0.101	0.102	-0.099	0.0108	0.0205	-0.0301
		Magnitude error (%)	1.00	2.00	1.00	8.00	2.50	0.33
Multi-frequent test	15.6 (Hz)	Target value	15.6	25	1	13	18	10
		Actual value	15.625	25.004	1.044	13.018	18.014	10.014
		Error (%)	0.16	0.02	0.44	0.14	0.08	0.14
	46.8 (Hz)	Target value	46.8	4	16	22	4	6
		Actual value	46.875	4.0165	16.007	22.019	4.0254	6.009
		Error (%)	0.16	0.41	0.04	0.09	0.64	0.15
	100 (Hz)	Target value	100	5	3	2	4	1
		Actual value	100	5.0898	3.1087	2.0661	4.0167	1.0123
		Error (%)	0.00	1.80	3.62	3.31	0.42	1.23

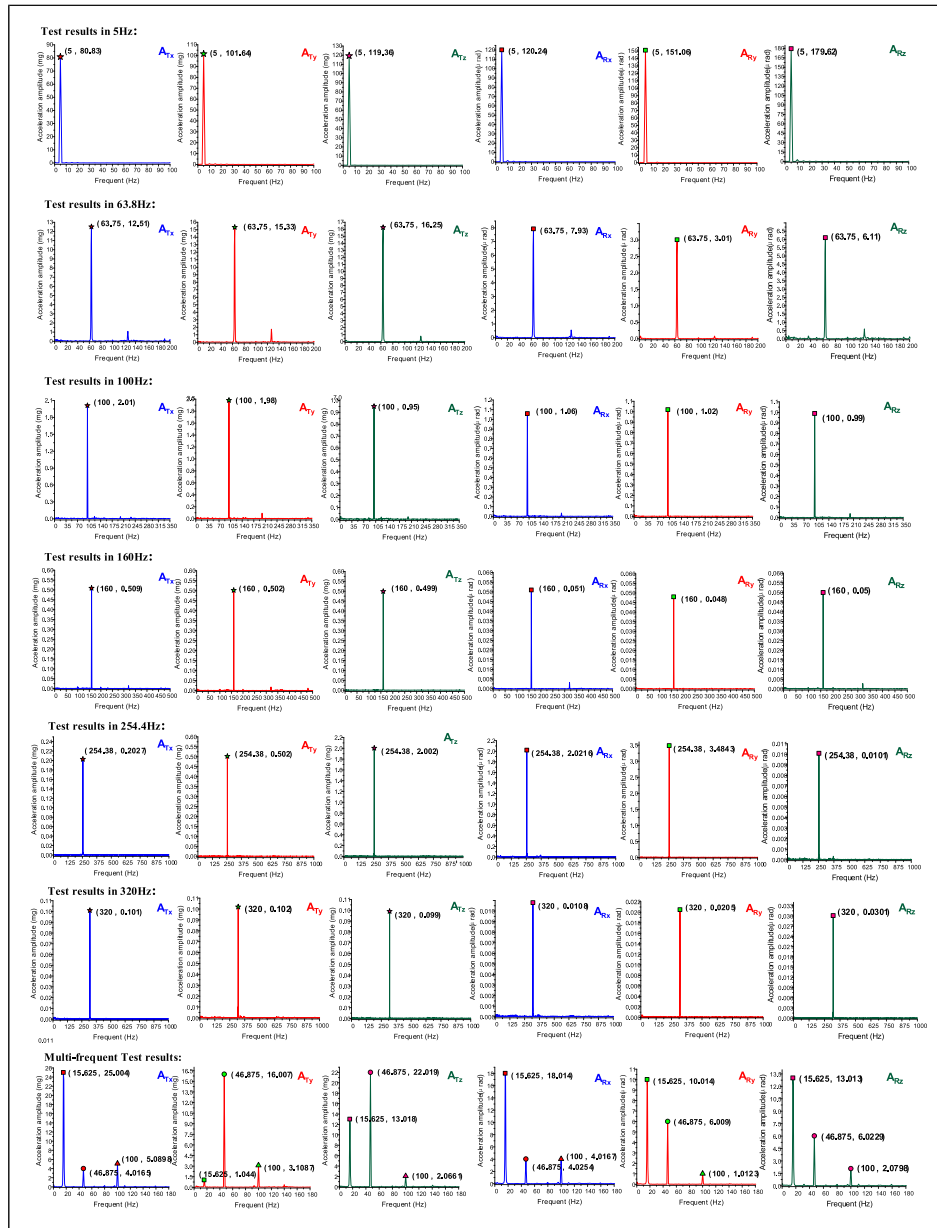


Figure 12. The test frequency domain curves.

It can be seen from Table 3 that the output vibration bandwidth of the simulator is 5–320 Hz, the translational vibration magnitude is 0.1 mg–120 mg, the rotational vibration magnitude is 0.01 μ rad–180 μ rad, the maximum magnitude error of single frequency experiment is 8% appearing in X-axis angular acceleration at 320 Hz and the maximum magnitude error of multi-frequency experiment is 4.99% appearing in Z-axis angular acceleration at 100 Hz, and the frequent error is caused by the setting of sampling

frequency. Figure 12 shows the acceleration frequency domain curves. The results of single-frequency micro-vibration tests results are shown in first six lines, and the multi-frequency test results with 3 frequencies tested simultaneously are shown in line 7, which shows that the simulator proposed in this paper can accurately simulate the 6-DOF micro-vibration. But there is frequency doubling phenomenon at some frequencies which might be caused by the GSP’s joint-clearances and the non-linearity

of the spring leaf axial stiffness. At present, the frequency doubling phenomenon has not been dealt well with, and how to suppress from the structural design and control strategy will be further studied in the future.

5. Conclusions

In this paper, a space micro-vibration simulation platform based on improved GSP is designed to satisfy the requirement of vibration sources simulation in the ground test of the on-orbit optical load, which has the characteristics that include large frequent bandwidth, high load carrying capacity, and small vibration magnitude. The natural frequency calculation formula is deduced by dynamic modeling. The structure of the single-axial actuator is designed and optimized according to the optimal configuration, which obtained that the first 6-order radical frequency of the platform is less than 3.5 Hz, and the 7th-order radical frequency was more than 354 Hz. The transfer function is used to control the simulator and experiment results show that the output bandwidth of the simulator is 5–300 Hz, the translational vibration magnitude is 0.1 mg–120 mg, the rotational vibration magnitude is 0.01 μ rad–180 μ rad, and the maximum error of magnitude is 8%. In the future, we will further study how to suppress frequency doubling phenomenon from the structure design and control strategy.


Declaration of conflicting interests

The author(s) declared no potential conflicts of interest with respect to the research, authorship, and/or publication of this article.

Funding

The author(s) disclosed receipt of the following financial support for the research, authorship, and/or publication of this article: This work was supported by the Jilin Scientific and Technological Development Program [grant number 20200404204YY]; Key-Area Research and Development Program of Guangdong Province [grant number 2020B0404020002].

ORCID iDs

He Zhu  <https://orcid.org/0000-0002-6539-9601>
 Shuai He  <https://orcid.org/0000-0003-0992-0500>
 Xiangyang Sun  <https://orcid.org/0000-0003-1868-559X>

References

- Cui Y, Feng Z and Liu J (2019) Micro-vibration influencing characteristic on image quality and solutions for high-resolution satellites. *Advances in Astronautics Science and Technology* 2: 1–7. DOI: [10.1007/s42423-019-00033-1](https://doi.org/10.1007/s42423-019-00033-1)
- Hadar O, Fisher M and Kopeika NS (1992) Image resolution limits resulting from mechanical vibrations. Part III: numerical calculation of modulation transfer function. *Optical Engineering* 31(3): 581–589. DOI: [10.1117/12.7974110](https://doi.org/10.1117/12.7974110)
- He S, Xu Z, Wang X, et al. (2017) *Design and Testing of a Parallel Manipulator for Space Micro-vibration Simulation//Annual Conference towards Autonomous Robotic Systems*. Cham: Springer. DOI: [10.1007/978-3-319-64107-28](https://doi.org/10.1007/978-3-319-64107-28)
- Joshi A and Kim WJ (2004) System identification and multi-variable control design for a satellite ultraquiet isolation technology experiment (suite). *European Journal of Control* 10(2): 174–186. DOI: [10.3166/ejc.10.174-186](https://doi.org/10.3166/ejc.10.174-186)
- Laski RA and Martin MS (1989) Control/structure system design of a spaceborne optical interferometer. Proceedings of the AAS/AIAA Astrodynamics Specialist Conference. Minneapolis, Minnesota: 369–395.
- Lee-Glauser GJ (1994) Vibration control of spacecrafts and space structures from lift-off to on-orbit environments. DOI: [10.1177/026635119300800302](https://doi.org/10.1177/026635119300800302)
- Le TD and Ahn KK (2013) Experimental investigation of a vibration isolation system using negative stiffness structure. *International Journal of Mechanical Sciences* 70(5): 99–112. DOI: [10.1016/j.ijmecsci.2013.02.009](https://doi.org/10.1016/j.ijmecsci.2013.02.009)
- Liu C, Jing X, Daley S, et al. (2015) Recent advances in micro-vibration isolation. *Mechanical Systems and Signal Processing* 56-57: 55–80. DOI: [10.1016/j.ymsp.2014.10.007](https://doi.org/10.1016/j.ymsp.2014.10.007)
- Lin L, Tan L, Lin K, et al. (2018) The influence of flywheel micro vibration on space camera and vibration suppression. *Mechanical Systems and Signal Processing* 100: 360–370. DOI: [10.1016/j.ymsp.2017.07.029](https://doi.org/10.1016/j.ymsp.2017.07.029)
- Park G, Lee DO, Han JH, et al. (2012) Development of multi-DOF active microvibration emulator. In: ASME Conference on Smart Materials, Georgia, USA, 19–21 September 2012, pp. 477–483. DOI: [10.1115/SMASIS2012-8240](https://doi.org/10.1115/SMASIS2012-8240)
- Park G, Lee DO and Han JH (2014) Development of multi-degree-of-freedom microvibration emulator for efficient fitter test of spacecraft. *Journal of Intelligent Material Systems and Structures* 25(9): 1069–1081. DOI: [10.1177/1045389X14523852](https://doi.org/10.1177/1045389X14523852)
- Shao Z, Tang X, Xu C, et al. (2012) Research on the inertia matching of the Stewart parallel manipulator. *Robotics and Computer Integrated Manufacturing* 28(6): 649–659. DOI: [10.1016/j.rcim.2012.04.001](https://doi.org/10.1016/j.rcim.2012.04.001)
- Serief C (2017) Estimate of the effect of micro-vibration on the performance of the Algerian satellite (Alsat-1B) imager. *Optics Laser Technology* 96: 147–152. DOI: [10.1016/j.optlastec.2017.05.035](https://doi.org/10.1016/j.optlastec.2017.05.035)
- Tang X and Shao Z (2013) Trajectory generation and tracking control of a multi-level hybrid support manipulator in fast. *Mechatronics* 23(8): 1113–1122. DOI: [10.1016/j.mechatronics.2013.09.002](https://doi.org/10.1016/j.mechatronics.2013.09.002)
- Verma M, Lafarga V, Dehaeze T, et al. (2020) Multi-degree of freedom isolation system with high frequency roll-off for drone camera stabilization. *IEEE Access* 8: 176188–176201. DOI: [10.1109/ACCESS.2020.3027066](https://doi.org/10.1109/ACCESS.2020.3027066)
- Vose TH, Umbanhowar P and Lynch KM (2009) Friction-induced velocity fields for point parts sliding on a rigid oscillated plate. *International Journal of Robotics Research* 28(8): 1020–1039. DOI: [10.1177/0278364909340279](https://doi.org/10.1177/0278364909340279)
- Vose TH, Turpin MH, Dames PM, et al. (2013) Modeling, design, and control of 6-DOF flexure-based parallel mechanisms for vibratory manipulation. *Mechanism and Machine Theory* 64: 111–130. DOI: [10.1016/j.mechmachtheory.2012.12.007](https://doi.org/10.1016/j.mechmachtheory.2012.12.007)
- Wang X, Xu Z, He S, et al. (2017) Modeling and analysis of a multi-degree-of-freedom micro-vibration simulator. *Shock and Vibration* 2017(4): 1–17. DOI: [10.1155/2017/4840514](https://doi.org/10.1155/2017/4840514)
- Wang X, Xu Z, Xia M, et al. (2018) Research on a six-degree-of-freedom disturbance force and moment simulator for space

- micro-vibration experiments. *Journal of Sound and Vibration* 432: 530–548. DOI: [10.1016/j.jsv.2018.06.056](https://doi.org/10.1016/j.jsv.2018.06.056)
- Whiteman WE and Berman MS (2014) Fatigue failure results for multi-axial versus uniaxial stress screen vibration testing. *Shock and Vibration* 9(6): 319–328. DOI: [10.1155/2002/109715](https://doi.org/10.1155/2002/109715)
- Wu D, Xie T, Lu M, et al. (2019) Modeling and experimental study on the micro-vibration transmission of a control moment gyro[J]. *IEEE Access* 99: 1–1. DOI: [10.1109/ACCESS.2019.2922705](https://doi.org/10.1109/ACCESS.2019.2922705)
- Xin J, Xu Z, Yang J, et al. (2015) Dynamic analysis and test of a space micro-vibration simulator based on 6-dimensional parallel mechanism[J]. *Robot* 37(5): 581–587. DOI: [10.13973/j.cnki.robot.2015.0581](https://doi.org/10.13973/j.cnki.robot.2015.0581)
- Yang J, Xu Z, Wu Q, et al. (2016) Dynamic modeling and control of a 6-DOF micro-vibration simulator[J]. *Mechanism and Machine Theory* 104: 350–369. DOI: [10.1016/j.mechmachtheory.2016.06.011](https://doi.org/10.1016/j.mechmachtheory.2016.06.011)
- Zhou W, Aglietti GS and Zhang Z (2011) Modelling and testing of a soft suspension design for a reaction/momentum wheel assembly. *Journal of Sound and Vibration* 330(18): 4596–4610. DOI: [10.1016/j.jsv.2011.03.028](https://doi.org/10.1016/j.jsv.2011.03.028)
- Zhou W, Liu D, Luo Q, et al. (2012) Analysis and testing of microvibrations produced by momentum wheel assemblies[J]. *Chinese Journal of Aeronautics* 25(4): 640–649. DOI: [10.1016/S1000-9361\(11\)60430-5](https://doi.org/10.1016/S1000-9361(11)60430-5)
- Zhou W and Liu D (2013) Experimental research on a vibration isolation platform for momentum wheel assembly. *Journal of Sound and Vibration* 332(5): 1157–1171. DOI: [10.1016/j.jsv.2012.10.027](https://doi.org/10.1016/j.jsv.2012.10.027)
- Zhu H, He S, Xu Z, et al. (2022) Iterative feedback control based on frequency response model for a six-degree-of-freedom micro-vibration platform. *Journal of Vibration and Control* 28(13–14): 1727–1738. DOI: [10.1177/1077546321997310](https://doi.org/10.1177/1077546321997310)